 CMC, vol.5, no.2, pp.129-150, 2007

A Numerical Study of Strain Localization in Elasto-Thermo-Viscoplastic Materials using Radial Basis Function Networks

P. Le[1] **N. Mai-Duy**[1] **T. Tran-Cong**[1] **and G. Baker**[2]

Abstract: This paper presents a numerical simulation of the formation and evolution of strain localization in elasto-thermo-viscoplastic materials (adiabatic shear band) by the indirect/integral radial basis function network (IRBFN) method. The effects of strain and strain rate hardening, plastic heating, and thermal softening are considered. The IRBFN method is enhanced by a new coordinate mapping which helps capture the stiff spatial structure of the resultant band. The discrete IRBFN system is integrated in time by the implicit fifth-order Runge-Kutta method. The obtained results are compared with those of the Modified Smooth Particle Hydrodynamics (MSPH) method and Chebychev Pseudo-spectral (CPS) method.

Keyword: Shear band, strain localization, RBFN, imperfection, shear band formation.

1 Introduction

Strain localization in elasto-thermo-visco-plastic materials is a phenomenon that occurs during high strain-rate plastic deformation, such as machining, forging, shock impact loading, ballistic impact and penetration, and has been proposed as an explanation for deep earthquakes [Walter (1992)]. In particular, a shear band is a narrow, nearly planar or two dimensional region of very large shear strain and strain rate. The formation of shear bands often precedes the rupture in materials. Even when the rupture does not occur, the development of shear bands generally reduces the performance of the material. Hence, an understanding of shear-band morphology and evolution is an important prerequisite to improve material processes and manufacturing techniques. Shear bands are commonly of isothermal or adiabatic types [Molinari and Clifton (1987)]. Isothermal shear bands form as a result of strain softening, and thermal softening plays a negligible role in the process. On the other hand, adiabatic shear bands, in which thermal softening plays a primary role, form as a result of an autocatalytic process: an increase in strain rate in a weaker zone causes a local increase in temperature which in turn creates a further increase in strain rate. Once a band is fully formed, the two sides of the region are displaced relative to each other, much like a mode II or mode III crack, but the material still retains full physical continuity from one side to the other.

This paper focuses on adiabatic shear bands. The equations governing the evolution of adiabatic shear bands are coupled, highly nonlinear and stiff, and it is not simple, even for one-dimensional problems, to obtain close form solutions that could describe a range of constitutive, boundary, and initial conditions. For a number of special cases, close form exact and approximate solutions have been developed by many authors, for example [Rice and Rudnicki (1980); Molinari and Clifton (1987); Wright (1990); Sherif and Shawki (1992)], just to name a few, to capture some of the fundamental characteristics of strain localization. Generally, numerical solutions are helpful in a parametric study to cover a range of possible behaviours. However, it could be costly to resolve shear bands fully in a large scale computation since the morphology of a shear band exhibits very fine transverse scales, with aspect ratios of the high shear region usually in the hundreds or even thousands [Wright (2002)]. Thus it is highly desirable to have effective and efficient numerical methods for the analysis of strain localisation problems. The spectral method [Bayliss,

[1] CESRC, University of Southern Queensland, Toowoomba, QLD 4350, Australia.
[2] DVC(S), University of Southern Queensland, Toowoomba, QLD 4350, Australia.

Belytschko, Kulkarni, and Lott-Crumpler (1994)] is particularly effective and efficient, but generally restricted to simple geometries. The finite element method (FEM) [Wright and Walter (1987); Batra and Kim (1991); Walter (1992)] has been used to analyze shear strain localization problems with good results for 1D cases, since the Lagrangian finite element mesh is not badly distorted and small element size of $O(10^{-7})$ enables one to capture the high strain. However, the FEM has many drawbacks in 2D or 3D strain localization problems. In contrast to the FEM, meshless methods [Atluri and Zhu (1998); Li and Liu (2000); Batra and Zhang (2004); Atluri and Shen (2002); Han and Atluri (2003); Han and Atluri (2004); Han, Rajendran, and Atluri (2005); Han, Liu, Rajendran, and Atluri (2006)] offer some advantages, including (i) shape functions are constructed by using a highly smooth window function, (ii) purely displacement-based formulation is possible without incurring volumetric locking within a range of support size of the window functions [Li and Liu (2000)], and (iii) approximations are non-local. Thus, meshless methods provide more continuous solutions than the piece-wise continuous ones obtained by the FEM. These properties provide an effective remedy for the mesh alignment sensitivity in the computation of strain localization.

In this study, we report a new numerical method based on radial basis function networks, a truly meshless method, for analysis of the dynamics of strain localization in 1D problems. The present indirect/integral radial basis function network (IRBFN) method is based on (i) the universal approximation property of RBF networks, (ii) exponential convergence characteristics of the chosen multiquadric (MQ) RBF, (iii) a simple point collocation method of discretisation of the governing equations, and (iv) an indirect/integral (IRBFN) rather than a direct/differential (DRBFN) approach [Kansa (1990)] for the approximation of functions and derivatives. For the DRBFN, Madych and Nelson (1990) showed that the convergence rate is a decreasing function of derivative order. Since the introduction of the IRBFN approach by [Mai-Duy and Tran-Cong (2001); Mai-Duy and Tran-Cong (2005)], Kansa, Power, Fasshauer, and Ling (2004), and Ling and Trummer (2004), based on the theoretical result of Madych and Nelson (1990), concluded that the decreasing rate of convergence can be avoided in the IRBFN approach. Furthermore, the integration constants arisen in the IRBFN approach are helpful in dealing with problems with multiple boundary conditions [Mai-Duy and Tran-Cong (2006)]. In addition, a new coordinate mapping is here introduced to help capture the characteristics of extremely thin boundary layers (i.e. the localised shear bands). The paper is organized as follows. The physical problem and its mathematical model are defined in section 2. The numerical formulation of the mathematical model is presented in section 3 which is followed by numerical examples in section 4. Some conclusions are drawn in section 5.

2 Problem definition

We consider the unidirectional shearing of an infinite slab of half thickness $\overline{H}$, and of an elasto-thermo-viscoplastic material. In this section we use the overbar to represent dimensional quantities, the subscript comma to denote the partial differentiation with respect to the variable indicated by the subscript. The unknowns are the shear stress $\overline{s}$, the particle velocity $\overline{v}$, the plastic strain γ and the temperature measured from the reference value $\overline{\Theta}$. In addition, the strain hardening parameter Ψ is also introduced as in [Walter (1992); Bayliss, Belytschko, Kulkarni, and Lott-Crumpler (1994)].

Let $\overline{y}$ be the coordinate across the slab with origin on the middle plane, i.e. $-\overline{H} \leq \overline{y} \leq \overline{H}$, and $\overline{t}$ denote time. The mathematical model for this problem can be found in [Walter (1992); Wright (2002); Bayliss, Belytschko, Kulkarni, and Lott-Crumpler (1994)] and is reproduced here as follows.

$$\overline{v}_{,\overline{t}} = \frac{\overline{s}_{,\overline{y}}}{\overline{\rho}}, \tag{1a}$$

$$\overline{s}_{,\overline{t}} = \overline{\mu}(\overline{v}_{,\overline{y}} - \overline{\gamma}_{,\overline{t}}), \tag{1b}$$

$$\overline{\rho c}\dot{\overline{\Theta}} = \overline{k}\overline{\Theta}_{,\overline{y}\overline{y}} + \overline{s}\overline{\gamma}_{,\overline{t}}, \tag{1c}$$

$$\overline{\Psi}_{,\overline{t}} = \frac{\overline{s}\overline{\gamma}_{,\overline{t}}}{\overline{\kappa}(\Psi)}, \tag{1d}$$

where $\overline{\rho}$ is the density, $\overline{c}$ the specific heat, $\overline{k}$ the thermal conductivity, $\overline{\mu}$ the shear modulus, and $\overline{\kappa}$ a strain hardening factor. The constitutive relation between $\overline{s}$, Ψ, $\overline{\Theta}$ and $\overline{\gamma}_{,\overline{t}}$ is given by

$$\overline{s} = \overline{\kappa}(\Psi) g(\overline{\Theta}) f(\overline{\gamma}_{,\overline{t}}), \tag{2}$$

where g a thermal softening factor, and f a strain rate hardening factor. Different material models can be obtained with appropriate choices of these factors, which will be illustrated when we consider examples in section 4. The problem is assumed to be symmetric about the middle plane $\overline{y} = 0$. The slab is subjected to a constant shearing velocity $\pm\overline{v}^0$ prescribed at the top and bottom surfaces of the slab, respectively. The surfaces are thermally insulated and all plastic work is converted into heat. The above assumptions lead to the following boundary conditions

$$\begin{aligned} &\overline{v}(0,\overline{t}) = 0, \quad \overline{v}(\overline{H},\overline{t}) = \overline{v}_0, \\ &\overline{\Theta}_{,\overline{y}}(0,\overline{t}) = 0, \quad \overline{\Theta}_{,\overline{y}}(\overline{H},\overline{t}) = 0. \end{aligned} \tag{3}$$

The nominal strain rate is

$$\dot{\overline{\gamma}}^0 = \overline{\gamma}^0_{,\overline{t}} = \frac{\overline{v}^0}{\overline{H}}, \tag{4}$$

where the time derivatives are from now on indicated by a dot over the variable. The variables are non-dimensionalised as follows.

$y = \frac{\overline{y}}{\overline{H}}$, $t = \overline{t}\dot{\overline{\gamma}}^0$, $\dot{\Psi} = \frac{\dot{\overline{\Psi}}}{\dot{\overline{\gamma}}^0}$, $v = \frac{\overline{v}}{\overline{H}\dot{\overline{\gamma}}^0}$, $s = \frac{\overline{s}}{\overline{\kappa}^0}$,
$\Theta = \frac{\overline{\rho c}\overline{\Theta}}{\overline{\kappa}^0}$, $\kappa = \frac{\overline{\kappa}}{\overline{\kappa}^0}$, $\dot{\gamma} = \frac{\dot{\overline{\gamma}}}{\dot{\overline{\gamma}}^0}$, $k = \frac{\overline{k}}{\overline{\rho c}\overline{H}^2\dot{\overline{\gamma}}^0}$,
$\rho = \frac{\overline{\rho}\overline{H}^2(\dot{\overline{\gamma}}^0)^2}{\overline{\kappa}^0}$, $\mu = \frac{\overline{\mu}}{\overline{\kappa}^0}$, $b = \overline{b}\dot{\overline{\gamma}}^0$, $a = \frac{\overline{a}\overline{\kappa}^0}{\overline{\rho c}}$,

where $\overline{a}$ is the thermal softening parameter, $\overline{b}$ is the strain-rate hardening parameter, $\overline{\kappa}_0$ is the yield stress in the quasi-static isothermal simple shear test. The dimensionless governing equations are given by

$$\dot{v} = \frac{s_{,y}}{\rho}, \tag{5a}$$

$$\dot{s} = \mu(v_{,y} - \dot{\gamma}), \tag{5b}$$

$$\dot{\Theta} = k\Theta_{,yy} + s\dot{\gamma}, \tag{5c}$$

$$\dot{\Psi} = \frac{s\dot{\gamma}}{\kappa(\Psi)}. \tag{5d}$$

The constitutive relation is

$$s = \kappa(\Psi) g(\Theta) f(\dot{\gamma}). \tag{6}$$

The boundary conditions are

$$\begin{aligned} &v(0,t) = 0, \quad v(1,t) = 1, \\ &\Theta_{,y}(0,t) = 0, \quad \Theta_{,y}(1,t) = 0. \end{aligned} \tag{7}$$

From Eq. 5a and Eq. 7, the boundary conditions for shear stress can be found easily as

$$s_{,y}(0,t) = 0, \quad s_{,y}(1,t) = 0. \tag{8}$$

We will present a meshless numerical method for solving Eq. 5a-Eq. 8 in the next section, and in section 4 we will present results for two particular models, namely the thermal imperfection and the strength imperfection cases.

3 Numerical formulation

Consider an initial-boundary-value problem governed by the second order PDE

$$\frac{\partial u}{\partial t} = a\frac{\partial^2 u}{\partial x^2} + b\frac{\partial u}{\partial x} + cu + d, \tag{9}$$

where a, b, c and d are the coefficients, $0 \le t \le T$ and $x_{min} \le x \le x_{max}$, with the boundary and initial conditions

$$u(t, x_{min}) = u_1, \tag{10}$$

$$\frac{\partial u}{\partial x}\Big|_{(t,x=x_{max})} = u'_N, \tag{11}$$

$$u(0,x) = g(x), \tag{12}$$

in which u_1 and u'_N are given values, and $g(x)$ is a known function.

3.1 Spatial discretisation

In the indirect RBF method (see [Mai-Duy and Tran-Cong (2001); Mai-Duy and Tran-Cong (2005); Mai-Duy (2005); Mai-Duy and Tanner (2005)]), the formulation of the problem starts with the decomposition of the highest order derivative under consideration into RBFs. The derivative expression obtained is then integrated to yield expressions for lower order derivatives and finally for the original function itself. The present work is concerned with the approximation of a function and its derivatives of order up to 2, the formulation can be thus described as follows [Mai-Cao and Tran-Cong (2005)]

$$\frac{d^2u(x,t)}{dx^2} = \sum_{i=1}^{m} w_i(t) g_i(x) = \sum_{i=1}^{m} w_i(t) H_i^{[2]}(x), \tag{13}$$

$$\begin{aligned} \frac{du(x,t)}{dx} &= \int \sum_{i=1}^{m} w_i(t) g_i(x) dx + c_1(t) \\ &= \sum_{i=1}^{m} w_i(t) \int g_i(x) dx + c_1(t) \\ &= \sum_{i=1}^{m} w_i(t) H_i^{[1]}(x) + c_1(t), \end{aligned} \tag{14}$$

$$\begin{aligned} u(x,t) &= \sum_{i=1}^{m} w_i(t) \int H_i^{[1]}(x) dx + c_1(t)x + c_2(t) \\ &= \sum_{i=1}^{m} w_i(t) H_i^{[0]}(x) + c_1(t)x + c_2(t), \end{aligned} \tag{15}$$

where m is the number of RBFs, $\{g_i(x)\}_{i=1}^m$ is the set of RBFs, $\{w_i(t)\}_{i=1}^m$ is the set of corresponding network weights to be found and $\{H_i^{[.]}(x)\}_{i=1}^m$ are new basis functions obtained from integrating the radial basis function $g_i(x)$. The multiquadrics function is chosen in the present study

$$g_i(x) = \sqrt{(x-c_i)^2 + a_i^2}, \tag{16}$$

where c_i is the RBF centre and a_i is the RBF width. The width of the i^{th} RBF can be determined according to the following simple relation

$$a_i = \beta d_i, \tag{17}$$

where β is a factor, $\beta > 0$, and d_i is the distance from the i^{th} centre to its nearest centre. To have the same coefficient vector as Eq. 15, expressions Eq. 13 and Eq. 14 can be rewritten as follows

$$\frac{d^2u(x,t)}{dx^2} = \sum_{i=1}^{m} w_i(t) H_i^{[2]}(x) + c_1(t).0 + c_2(t).0, \tag{18}$$

$$\frac{du(x,t)}{dx} = \sum_{i=1}^{m} w_i(t) H_i^{[1]}(x) + c_1(t).1 + c_2(t).0. \tag{19}$$

Here we choose the RBF centres c_i to be identical to the collocation points x_i, i.e. $\{c_i\}_{i=1}^m = \{x_i\}_{i=1}^N$. The evaluation of Eq. 18, Eq. 19 and Eq. 15 at a set of N collocation points leads to

$$\mathbf{u}''(t) = \mathbf{H}^{[2]}\mathbf{w}(t), \tag{20}$$

$$\mathbf{u}'(t) = \mathbf{H}^{[1]}\mathbf{w}(t), \tag{21}$$

$$\mathbf{u}(t) = \mathbf{H}^{[0]}\mathbf{w}(t), \tag{22}$$

where

$$\mathbf{u}''(t) = \left[\frac{\partial^2 u_1(t)}{\partial x^2}, \frac{\partial^2 u_2(t)}{\partial x^2}, \ldots, \frac{\partial^2 u_N(t)}{\partial x^2}\right]^T, \tag{23}$$

$$\mathbf{u}'(t) = \left[\frac{\partial u_1(t)}{\partial x}, \frac{\partial u_2(t)}{\partial x}, \ldots, \frac{\partial u_N(t)}{\partial x}\right]^T, \tag{24}$$

$$\mathbf{u}(t) = [u_1(t), u_2(t), \ldots, u_N(t)]^T, \tag{25}$$

$$\mathbf{H}^{[2]} = \begin{pmatrix} H_1^{[2]}(x_1) & H_2^{[2]}(x_1) & \cdots & H_N^{[2]}(x_1) & 0 & 0 \\ H_1^{[2]}(x_2) & H_2^{[2]}(x_2) & \cdots & H_N^{[2]}(x_2) & 0 & 0 \\ \vdots & \vdots & \ddots & \vdots & \vdots & \vdots \\ H_1^{[2]}(x_N) & H_2^{[2]}(x_N) & \cdots & H_N^{[2]}(x_N) & 0 & 0 \end{pmatrix}, \tag{26}$$

$$\mathbf{H}^{[1]} = \begin{pmatrix} H_1^{[1]}(x_1) & H_2^{[1]}(x_1) & \cdots & H_N^{[1]}(x_1) & 1 & 0 \\ H_1^{[1]}(x_2) & H_2^{[1]}(x_2) & \cdots & H_N^{[1]}(x_2) & 1 & 0 \\ \vdots & \vdots & \ddots & \vdots & \vdots & \vdots \\ H_1^{[1]}(x_N) & H_2^{[1]}(x_N) & \cdots & H_N^{[1]}(x_N) & 1 & 0 \end{pmatrix}, \tag{27}$$

$$\mathbf{H}^{[\mathbf{0}]} = \begin{pmatrix} H_1^{[0]}(x_1) & H_2^{[0]}(x_1) & \cdots & H_N^{[0]}(x_1) & x_1 & 1 \\ H_1^{[0]}(x_2) & H_2^{[0]}(x_2) & \cdots & H_N^{[0]}(x_2) & x_2 & 1 \\ \vdots & \vdots & \ddots & \vdots & \vdots & \vdots \\ H_1^{[0]}(x_N) & H_2^{[0]}(x_N) & \cdots & H_N^{[0]}(x_N) & x_N & 1 \end{pmatrix}, \tag{28}$$

and

$$\mathbf{w}(t) = [w_1(t), ..., w_N(t), c_1(t), c_2(t)]^T. \tag{29}$$

From an engineering point of view, it would be more convenient to work in the physical space. Owing to the presence of integration constants, the process of converting the networks-weight space into the physical space can also be used to implement Neumann boundary conditions. With the boundary conditions Eq. 10 and Eq. 11, the conversion system can be employed as

$$\begin{pmatrix} \mathbf{u}(t) \\ u'_N(t) \end{pmatrix} = \mathbf{C}\mathbf{w}(t), \tag{30}$$

where $\mathbf{C}$ is the conversion matrix of dimension $(N+1)\times(N+2)$ that comprises the matrix $\mathbf{H}^{[\mathbf{0}]}$ and the last row of $\mathbf{H}^{[\mathbf{1}]}$. Solving Eq. 30 yields

$$\mathbf{w}(t) = \mathbf{C}^{-1} \begin{pmatrix} \mathbf{u}(t) \\ u'_N(t) \end{pmatrix}. \tag{31}$$

By substituting Eq. 31 into Eq. 20 and Eq. 21, the values of the second and first derivatives of u with respect to x are thus expressed in terms of nodal variable values and Neumann boundary value

$$\mathbf{u}''(t) = \mathbf{H}^{[\mathbf{2}]}\mathbf{C}^{-1} \begin{pmatrix} \mathbf{u}(t) \\ u'_N(t) \end{pmatrix} = \mathbf{D}^{[\mathbf{2}]} \begin{pmatrix} \mathbf{u}(t) \\ u'_N(t) \end{pmatrix}, \tag{32}$$

$$\mathbf{u}'(t) = \mathbf{H}^{[\mathbf{1}]}\mathbf{C}^{-1} \begin{pmatrix} \mathbf{u}(t) \\ u'_N(t) \end{pmatrix} = \mathbf{D}^{[\mathbf{1}]} \begin{pmatrix} \mathbf{u}(t) \\ u'_N(t) \end{pmatrix}. \tag{33}$$

Making use of Eq. 32 and Eq. 33, equation Eq. 9 can be transformed into the following discrete form

$$\frac{d\mathbf{u}(t)}{dt} = a\mathbf{u}''(t) + b\mathbf{u}'(t) + c\mathbf{u}(t) + \mathbf{d}, \tag{34}$$

or

$$\frac{d\mathbf{u}}{dt} = a\mathbf{D}^{[\mathbf{2}]} \begin{pmatrix} \mathbf{u}(t) \\ u'_N(t) \end{pmatrix} + b\mathbf{D}^{[\mathbf{1}]} \begin{pmatrix} \mathbf{u}(t) \\ u'_N(t) \end{pmatrix} + c\mathbf{u}(t) + \mathbf{d}, \tag{35}$$

where $\mathbf{d} = [d, d, \ldots d]^T$ is an $N \times 1$ vector, and

$$\frac{d\mathbf{u}}{dt} = \left[\frac{du_1(t)}{dt}, \frac{du_2(t)}{dt}, \ldots, \frac{du_N(t)}{dt}\right]^T. \tag{36}$$

Since the values of u_1 and u'_N are given, the unknown vector becomes

$$[u_2(t), u_3(t), \ldots, u_N(t)]^T, \tag{37}$$

and hence, the first row in Eq. 35 will be removed from the solution procedure. The remainder of Eq. 35 can be integrated in time by using standard solvers such as the Runge-Kutta technique.

3.2 Resolution of very large spatial gradients

It has been shown that the IRBFN method can capture sharp gradients in some PDE solutions [Mai-Duy and Tran-Cong (2003)] with relatively coarse uniform spatial discretisation. However, with extremely sharp gradients in a solution, the option of uniformly refining the discretisation is not efficient or even effective. The computing of such extremely sharp gradients can be achieved effectively and efficiently with appropriate coordinate mappings of a relatively coarse, originally uniform discretisation. A very good mapping can be introduced as follows.

Consider the singularly perturbed boundary value problem (BVP)

$$\varepsilon u''(x) + p(x)u'(x) + q(x)u(x) = f(x), \quad \forall x \in [a,b], \tag{38}$$

subject to the boundary conditions

$$u(a) = u_a, \quad u(b) = u_b, \tag{39}$$

where $\varepsilon > 0$ denotes a fixed small constant. In many cases, Eq. 38 possesses boundary layers, i.e. regions of rapid change in the solution as $\varepsilon \longrightarrow 0$. Hence, in solving Eq. 38 with a point collocation method, the number of collocation points needs to be very large as $\varepsilon \longrightarrow 0$ to obtain an accurate solution. For a good resolution of the solution structure, at least one of collocation points must lie in the boundary layer [Tang and Trummer (1996); Ling and Trummer (2006)]. For example, if $\varepsilon \ll 1$ and the problem possesses a boundary

layer of width $O(\varepsilon)$, then on a uniform grid with $O(N^{-1})$ spacing between the points we would need $N = O(\varepsilon^{-1})$, which is not practical in most cases.

We transform the BVP Eq. 38 via the variable transformation $x \longmapsto y(x)$ into a new BVP

$$\varepsilon v''(y)\left[y'(x)\right]^2 + P(y)v'(y) + Q(y)v(y) = F(y), \quad \forall y \in [a,b], \quad (40)$$

subject to boundary conditions

$$v(a) = u_a, \quad v(b) = u_b, \quad (41)$$

where $v(y) = u(x(y))$, and the transformed coefficients are given by

$$P(y) = \varepsilon y''(x) + p(x)y'(x), \quad Q(y) = q(x), \quad F(y) = f(x). \quad (42)$$

In this mapping, x represents the physical space and y the computational space.

Without loss of generality, we assume that $[a,b] = [-1,1]$. Consider the one-to-one mapping given by

$$x(y) = \frac{\sinh(\alpha y)}{\sinh(\alpha)}, \quad (43)$$

where $\alpha > 0$ is a parameter that allows control of the discretisation, the smaller the value of ε is, the larger the value of α is required. From Eq. 43 the inverse mapping and the derivatives of y with respect to x can be determined simply

$$y(x) = \frac{\operatorname{arcsinh}(\lambda x)}{\alpha}, \quad (44)$$

$$y'(x) = \frac{\lambda}{(1+\lambda^2 x^2)^{\frac{1}{2}}\,\alpha}, \quad (45)$$

$$y''(x) = \frac{-\lambda^3 x}{(1+\lambda^2 x^2)^{\frac{3}{2}}\,\alpha}, \quad (46)$$

where $\lambda = \sinh(\alpha)$. As shown in the Figure 1(a), the physical space x is very dense around the layer's location $x = 0$ while the computational space y is uniform.

Note that the transform Eq. 43 also maps the interval $[-1,0]$ and $[0,1]$ onto themselves. Hence, if Eq. 38 has only one boundary layer on the left (or central or right), we can translate the physical space to $[-1,0]$ (or $[-1,1]$ or $[0,1]$) to avoid unnecessary collocation points in the non-steep region.

To illustrate the above mapping, we let $p(x) = 1$, $q(x) = 0$, $f(x) = x + 1 + \varepsilon$, $[a,b] = [0,1]$, $u_a = 0.5$ and $u_b = 1.5$ in Eq. 38, obtaining

$$\varepsilon u''(x) + u'(x) = x + 1 + \varepsilon, \quad \forall x \in [0,1], \quad u(0) = 0.5, \quad u(1) = 1.5, \quad (47)$$

which has an exact solution given by

$$u(x) = \frac{1}{2}\left(e^{-\frac{\varepsilon}{x}} + x^2 + 2x\right). \quad (48)$$

For $\varepsilon = 10^{-6}$, the IRBFN solution in the physical space with 61 collocation points, $\alpha = 13$, are shown in the Figure 1(b), which shows that the numerical solution is quite indistinguishable from the exact solutions. For $\varepsilon = 10^{-12}$, we can capture an accurate solution by using 161 collocation points and $\alpha = 29$.

4 Numerical examples

4.1 *Example 1: A model of thermal imperfection*

In this example we consider a specific case of the general unidirectional shearing problem defined in section 2 where the thermal softening factor in Eq. 6 is given by

$$g(\Theta) = (1 - a\Theta), \quad (49)$$

the strain hardening factor by

$$\kappa(\Psi) = \left(1 + \frac{\Psi}{\Psi^0}\right)^n, \quad (50)$$

and the strain rate hardening factor by

$$f(\dot{\gamma}) = (1 + b\dot{\gamma})^m. \quad (51)$$

For comparison purpose, the initial conditions and boundary conditions are taken to be the same as in Batra and Zhang (2004). The latter are described earlier by Eq. 7 and the former are given by

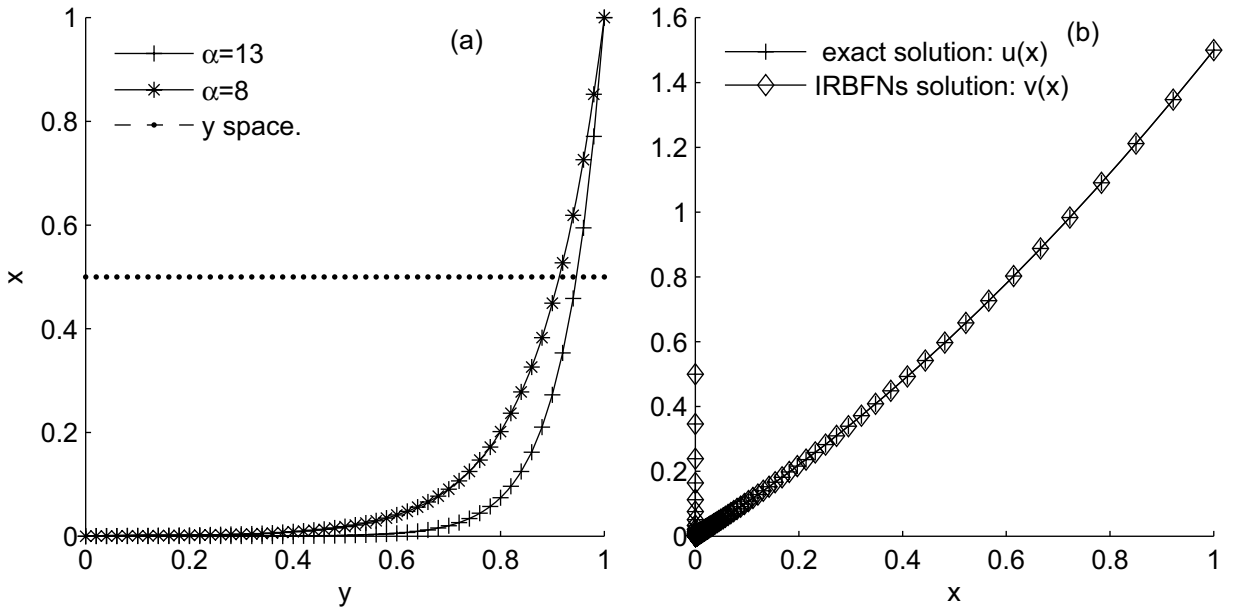

Figure 1: (a) Coordinate mapping with 61 collocation points, uniformly spaced in the computational space y, (b) IRBFN solution $v(x)$ and exact solution $u(x)$ of Eq. 47 with $\varepsilon = 10^{-6}$, $\alpha = 13$, on the physical space x.

$v(0,y) = y\,, \quad \Psi(0,y) = 0.1\,, \quad \gamma = 0.0692,$
$\Theta(0,y) = 0.1003 + 0.1(1-y^2)^9 e^{-5y^2}\,,$
$s(0,y) = \left(1+\frac{0.1}{\Psi^0}\right)^n (1-a\Theta(0,y))(1+b)^m,$
where the second term on the right-hand side of the expression for the temperature Θ represents a thermal imperfection. With the half thickness of the slab $\overline{H} = 2.58$mm, the nominal strain rate is $\overline{\gamma}_t^0 = 500\text{s}^{-1}$ and the dimensionless parameters are

$\rho = 3.982 \times 10^{-5}\,, \quad \mu = 240.3\,, \quad a = 0.4973\,,$
$n = 0.09\,, \quad \kappa = 3.978 \times 10^{-3}\,, \quad \Psi_0 = 0.017\,,$
$m = 0.025\,, \quad b = 5 \times 10^{-6}.$

The discretisation of the governing equations yields a system of fully coupled, stiff and nonlinear ordinary differential equations (ODEs) which are integrated with respect to time t using an implicit 5^{th} Runge-Kutta method with subroutine RADAU5 developed by Hairer, Norsett, and Wanner (1987), and Hairer and Wanner (1996). The subroutine automatically adjusts the time step size to compute the solutions within the prescribed accuracy. The results presented in this paper are obtained by setting $RTOL = 10^{-7}$ and $ATOL = 10^{-7}$ in RADAU5.

The results presented in this section are obtained with 261 collocation points and the value of α in the mapping Eq. 43 is 9, β in Eq. 17 is 1. The evolutions of the spatial profile of the temperature Θ, plastic strain γ, and strain hardening parameter Ψ, are shown in Figure 2; the plastic strain rate in Figure 3; stress and velocity in Figure 4. These figures show that the solution is highly consistent with the boundary conditions at $y = 0$ (and at $y = \pm 1$, although not shown on the plots). From Figure 2 it can be observed that the plastic strain increases rapidly in the neighbourhood of $y = 0$ where the band of high shear strains becomes less and less diffuse, reaching a minimum with a very high corresponding plastic strain level before becoming more and more diffuse again. Similar patterns of development are observed for the temperature, strain hardening parameter, plastic strain rate and velocity as shown in Figures 3 and 4. In contrast, the spatial profile of stress evolves slightly differently which will be discussed in more detail later.

Although banding of high shear strains is apparent, the smooth spatial profiles do not provide a clear and unique bandwidth. Thus we

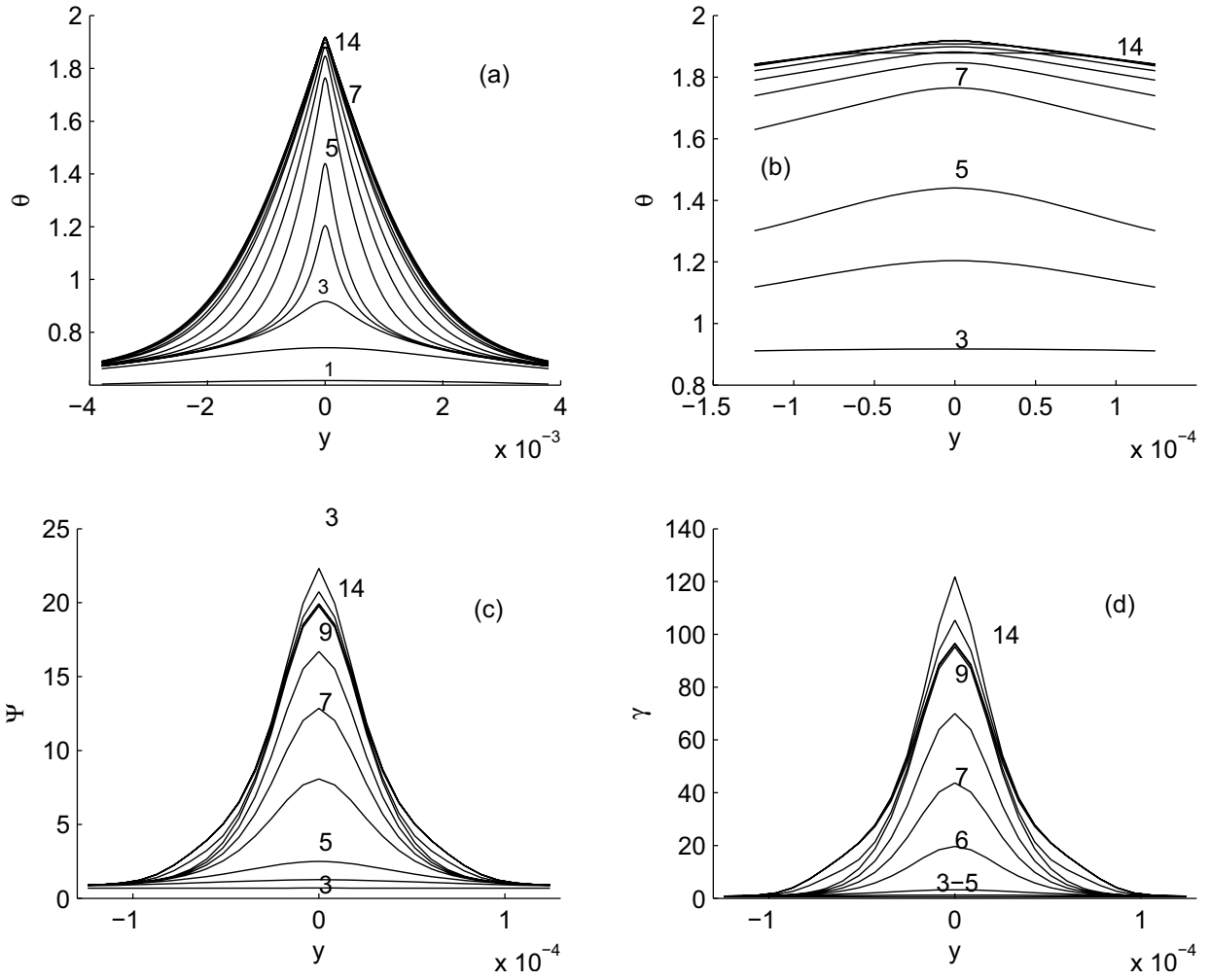

Figure 2: The curve labels indicate time levels (μs): 1(59.489); 2(60.257); 3(60.433); 4(60.477); 5(60.507); 6(60.602); 7(60.702); 8(60.804); 9(60.903); 10(60.934); 11(60.975); 12(60.992); 13(61.003); 14(61.019). (a) Evolution of temperature, (b) the temperature in the neighbourhood of $y = 0$ showing that the solution is highly consistent with the boundary conditions at $y = 0$, (c) evolution of Ψ, (d) evolution of plastic train.

define the limit of the high shear band as the position where the temperature equals 40% of the peak temperature at the centre of the band (This criterion is somewhat arbitrary, for example, Batra and Zhang (2004) used a value of 40% while Bayliss, Belytschko, Kulkarni, and Lott-Crumpler (1994) preferred 50%). The bandwidth evolves with time, for example when the plastic strain rate at $y = 0$ reaches its maximum value (at $t = 60.8385\mu$s), the extent of the corresponding bandwidth is $y = \pm 0.00252$. Hence the width of the shear band is $2 \times 0.00252 \times 2580 = 13.0\mu$m. The dimensionless half bandwidths correspond to different time levels (in parentheses) are 0.0688 (3),0.0257 (4),0.0102 (5),0.00279 (6),0.00237 (7),0.002468 (8),0.00264 (9),0.00274 (10),0.00276 (11), which indicate that the shear band becomes narrowest (around time level 7 or 60.702μs) before the plastic strain rate peaks between time levels 8 (60.804μs) and 9 (60.903μs).

Figures 5(a)-(d) show the evolution of the shear stress and temperature at $y = 0$. As can be seen in Figure 5(a), the shear stress initially increases slightly (from the initial value of 1.575) since strain and strain rate hardening effects are stronger than the thermal softening effect. As

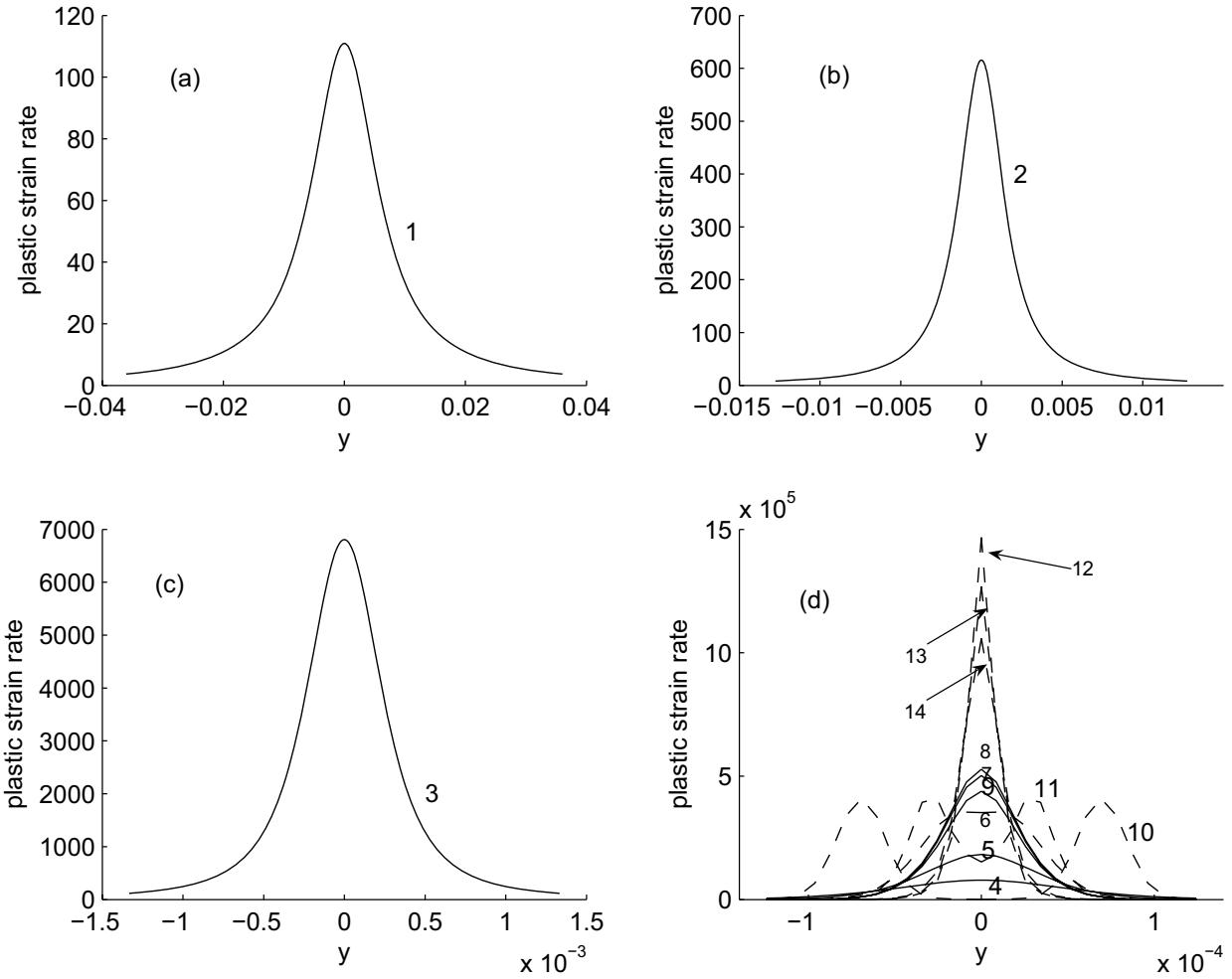

Figure 3: The evolution of plastic strain rate $\dot{\gamma}$. The curve labels indicate time levels (μs): 1(59.489); 2(60.257); 3(60.433); 4(60.477); 5(60.507); 6(60.602); 7(60.702); 8(60.804); 9(60.903); 10(60.934); 11(60.975); 12(60.992); 13(61.003); 14(61.019).

time progresses, the increase in plastic work causes increase in Θ and the thermal softening effect tends to compensate the strain and strain rate hardening effects. In the next phase of the evolution, Θ increases very slowly (Figure 5(c)) and the thermal softening effect becomes gradually stronger than strain and strain rate hardening effects, and the shear stress decreases very slowly as shown in Figure 5(a). Further evolutions of the stress and velocity profiles indicate unstable development, i.e. the shear stress at $y = 0$ is decreasing rapidly and the two halves of the slab (corresponding to $H \geq y > 0$ and $-H \leq y < 0$) are shearing relative to each other increasingly like rigid bodies. The instability can be seen more clearly by observing the evolution of shear stress (Figure 5) and plastic strain rate (Figure 6) at $y = 0$. The latter varies gradually and unremarkably up to $t = 60\mu$s, and shortly after which time, suddenly and steeply, i.e. by about five orders of magnitude in less than 0.5μs. After reaching the peak value of 5.3145×10^5 at $t = 60.8385\mu$s, the plastic strain rate quickly drops to a value very close to zero (i.e. 674 compared with the peak value of 5.3145×10^5) before showing a very small and slow increase, followed quickly by another sharp rise to a second peak (14.865×10^5) nearly three times the first one, as shown in Figure 6. Although the stress decreases rapidly and the plastic strain rate increases even more rapidly, the evo-

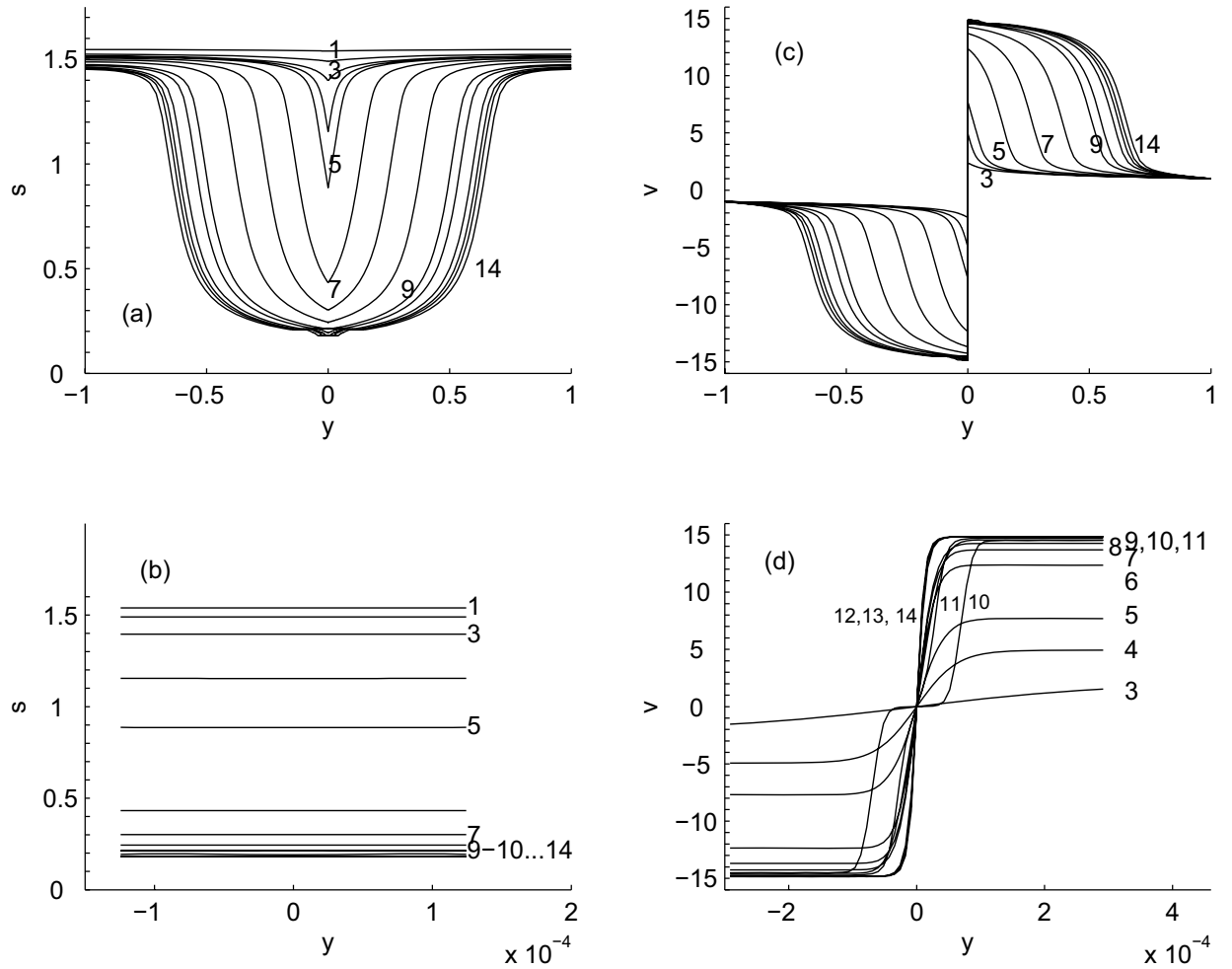

Figure 4: The curve labels indicate time levels (μs): 1(59.489); 2(60.257); 3(60.433); 4(60.477); 5(60.507); 6(60.602); 7(60.702); 8(60.804); 9(60.903); 10(60.934); 11(60.975); 12(60.992); 13(61.003); 14(61.019). (a) Spatial structure of shear stress at different times, (b) the shear stress in the neighbourhood of $y = 0$ showing that the solution is highly consistent with the boundary conditions at $y = 0$, (c) spatial structure of particles velocity at different times of localization, (d) the structure of the velocity boundary layer.

lution is smooth and therefore it is not possible to define the onset of instability uniquely. Here we define the onset of the strain localization instability as the point when the rate of change of stress with time continues to increase monotonically and rapidly. We detect this point by examining the ratio P defined as

$$P = \frac{\frac{ds}{dt}|_{t_{n+1}}}{\frac{ds}{dt}|_{t_n}}, \tag{52}$$

for several time levels n. The instability is thus found to occur at $t = 60.407\mu$s as shown in Figure 7. Figures 2, 3, 4 show that the interaction between the strain hardening and thermal softening effects, coupled with thermal diffusion and mechanical loading, gives rise to interesting mechanical response of the slab. The initially slow thermal diffusion, relative to the rate of mechanical loading, allows the thermal imperfection to cause local heating, which in turn causes thermal softening in a narrow band. As the thermal softening effect grows stronger than the strain and strain rate hardening effects, the plastic strain rate increases sharply and the shear stress drops suddenly at the band centre. Thermal diffusion also becomes more extensive and the extent of the soft-

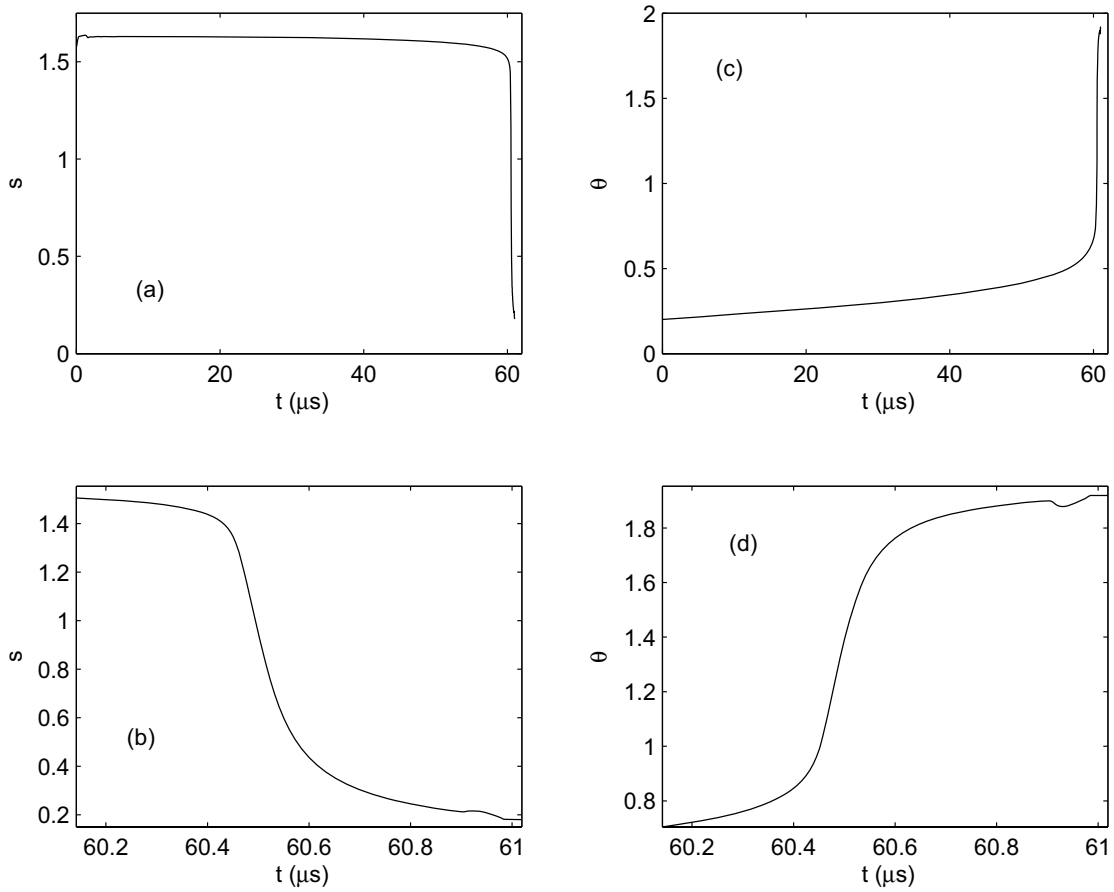

Figure 5: (a) and (b) evolution of shear stress at $y = 0$, (c) and (d) evolution of temperature at $y = 0$.

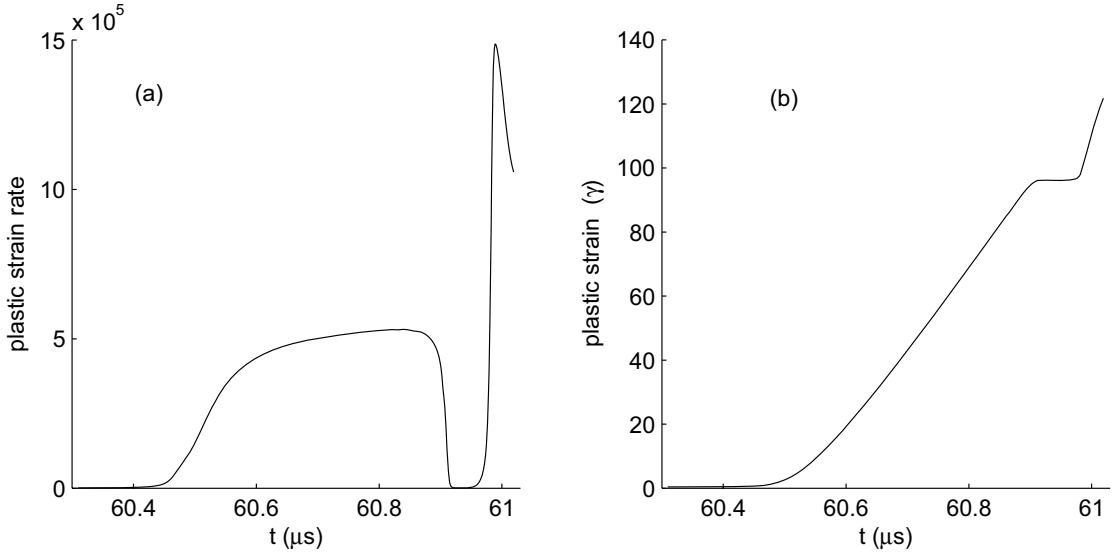

Figure 6: (a) Evolution of plastic strain rate $\dot{\gamma}$ at y =0, (b) evolution of plastic strain at $y = 0$.

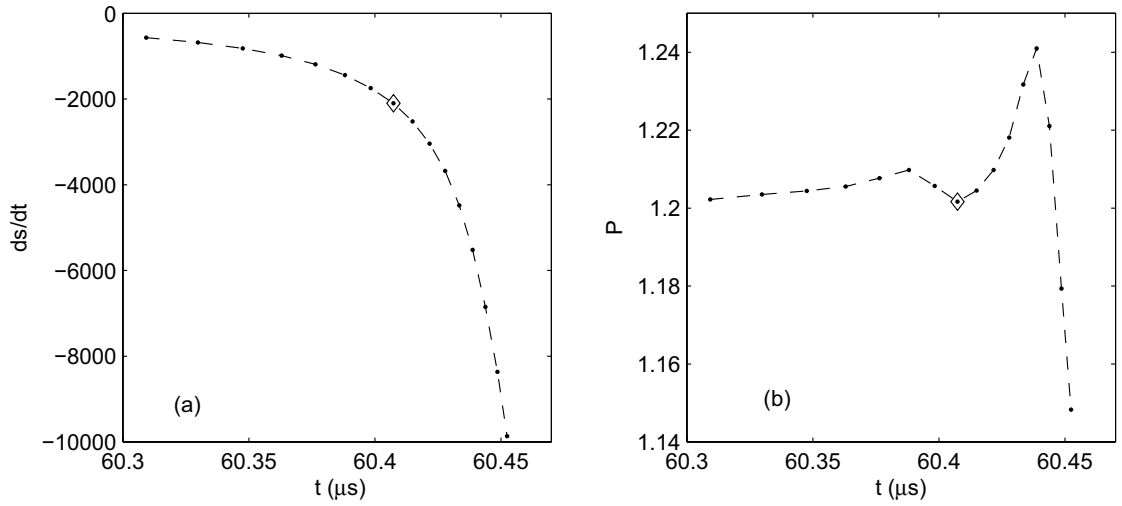

Figure 7: The behaviour of the shear stress at $y = 0$ around the onset of localisation. P is defined by Eq. 52.

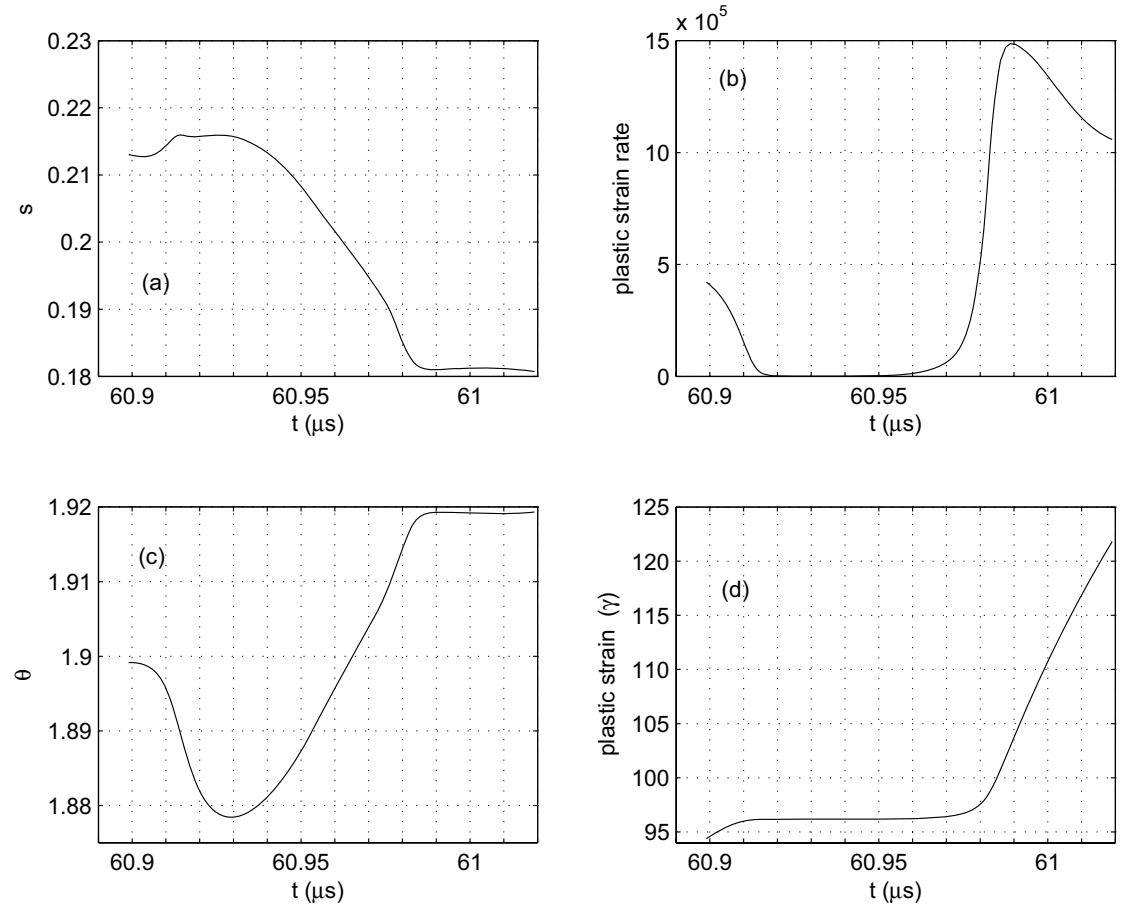

Figure 8: More detailed evolutions at $y = 0$.

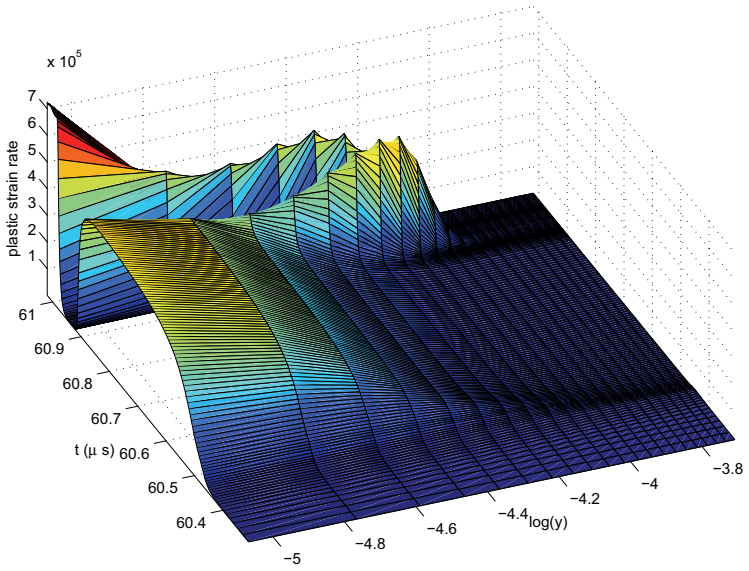

Figure 9: Evolution of the spatial profile of the plastic strain rate.

ened material propagates outwards as shown in Figure 4. Continued shearing of the slab after the onset of strain localization exhibits more interesting interaction between thermal softening and strain and strain rate hardening effects, giving rise to apparent elastic unloading in the neighbourhood of $y = 0$ as shown in Figures 8 and 9 while plastic deformation continues on either sides of the band centre as shown in Figure 3(d). However, high rate of plastic deformation quickly resumes as shown by the same figures.

4.2 *Example 2: A model of strength imperfection*

In this section, we consider another specific case of the general unidirectional shearing problem defined in section 2, where the strain rate hardening factor f is the same as in the previous example (i.e. given by Eq. 51), and the thermal softening factor in Eq. 2 is given by

$$g(\overline{\Theta}) = e^{-\overline{a}\overline{\Theta}}. \tag{53}$$

Following Bayliss, Belytschko, Kulkarni, and Lott-Crumpler (1994), the strain hardening factor $\overline{\kappa}(\Psi)$ in Eq. 1d is now taken as

$$\overline{\kappa}(\Psi) = \left(1 - 0.005(1-\overline{y}^2)^{50} e^{-500\overline{y}^2}\right) \overline{\kappa}_0 \left(1 + \frac{\Psi}{\Psi_0}\right)^n, \tag{54}$$

where the leading factor represents a strength imperfection. Eq. 53 and Eq. 54 are rewritten in dimensionless form as follows.

$$g(\Theta) = e^{-a\Theta}. \tag{55}$$

$$\kappa(\Psi) = \left(1 - 0.005(1-y^2)^{50} e^{-500y^2}\right) \left(1 + \frac{\Psi}{\Psi^0}\right)^n, \tag{56}$$

To compare the results of the present method with those obtained by other methods, we use the same parameters, boundary and initial conditions as in [Walter (1992); Bayliss, Belytschko, Kulkarni, and Lott-Crumpler (1994)]. The boundary conditions are described earlier by Eq. 7 and the initial conditions are

$$\begin{aligned} &v(0,y) = y, \quad s(0,y) = 0, \quad \gamma(0,y) = 0, \\ &\Theta(0,y) = 0.1(1-y^2)^9 e^{-5y^2}, \quad \Psi(0,y) = 0. \end{aligned} \tag{57}$$

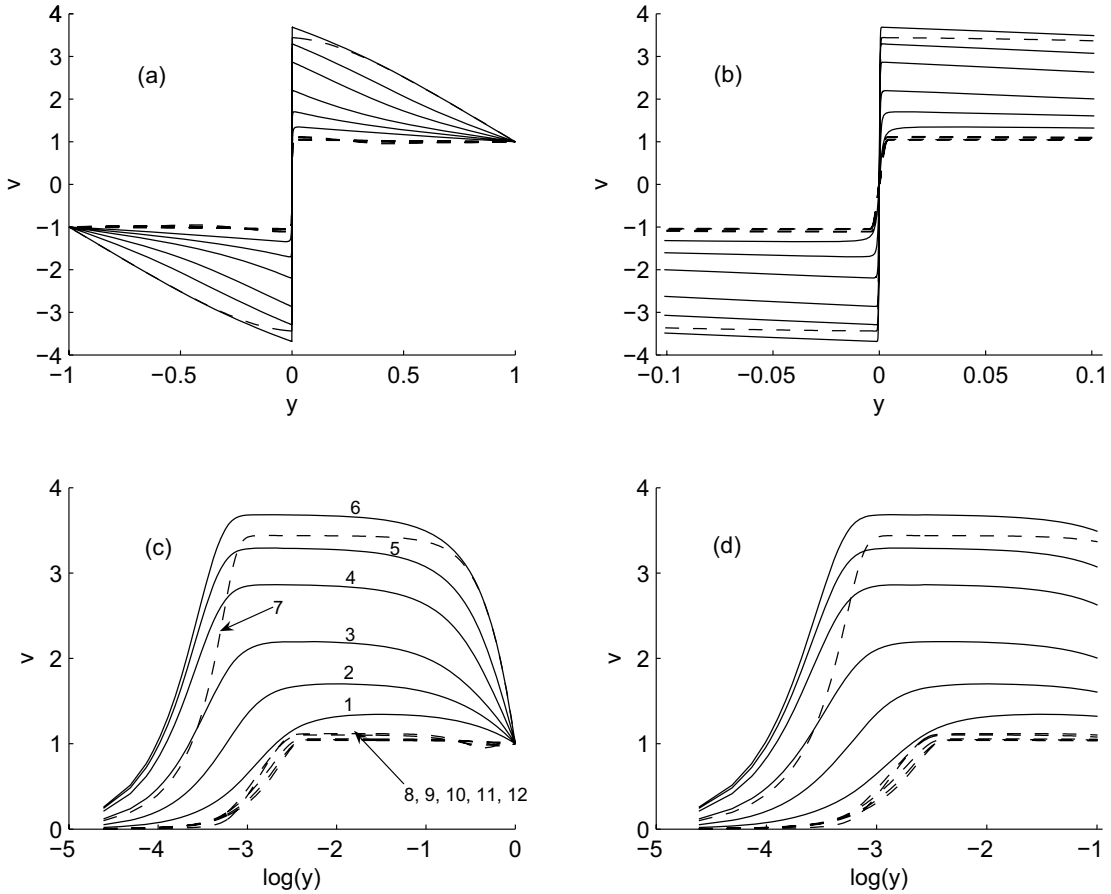

Figure 10: The spatial structure of particle velocity at selected points of time: (a) full linear scale, (c) semi-log scale $0 < y <= 1$, (b) behaviour in the neighbourhood of $y = 0$, linear scale, (d) behaviour in the neighbourhood of $y = 0$, semi-log scale $y > 0$. The band narrowing stage (the solid curves) includes instants of t = 0.76963(1), 0.77020(2), 0.77056(3), 0.77091(4), 0.77116(5), 0.77145(6) and the band widening or post-localization stage (the dash curves) includes instants t = 0.77254(7), 0.78364(8), 0.78815(9), 0.79408(10), 0.79763(11), 0.80000(12).

The half thickness of the slab $\overline{H}$ and the nominal strain rate $\dot{\overline{\gamma}}^0$ are taken as 3.47mm and 1000s^{-1}, respectively. Other parameters are

$\overline{\rho} = 7860\text{kgm}^{-3}$, $\overline{\mu} = 80\text{GPa}$, $\overline{\kappa}_0 = 602\text{MPa}$,
$\overline{a} = 6.43 \times 10^{-4}\text{s}^{-1}$, $\overline{b} = 1 \times 10^4\text{Js}^2(\text{kgm}^2)^{-1}$,
$\Psi_0 = 0.017$, $\overline{c} = 473\text{J}(\text{kg}^o\text{C})^{-1}$,
$\overline{k} = 49.2\text{J}(\text{ms}^o\text{C})^{-1}$, $m = 0.0251$, $n = 0.09$.

The results presented in this section are obtained with 221 collocation points, the value of α in the mapping Eq. 43 is 8 and β in Eq. 17 is 1. The results obtained here are in good qualitative agreement with those of Bayliss, Belytschko, Kulkarni, and Lott-Crumpler (1994), who also studied the sensitivity of the material response to imperfections. Figure 10 reveals the spatial structure of the particle velocity v at selected points of time, which shows that the strength imperfection (weakness) at the band centre leads to a fast process of softening in a narrow band around $y = 0$, manifested by a sudden and dramatic increase in the particle velocity due to the sudden drop in shear stress. The characteristics of shear banding are further exposed in Figure 11 which shows that plastic strain rate, plastic strain, temperature and stress are more or less constant within very narrow bands around $y = 0$. Figure 11 also shows that there are two evolutionary stages of the shear band. In the first stage, the band narrows up to time instant around $t = 0.77145$ (instant 6) and

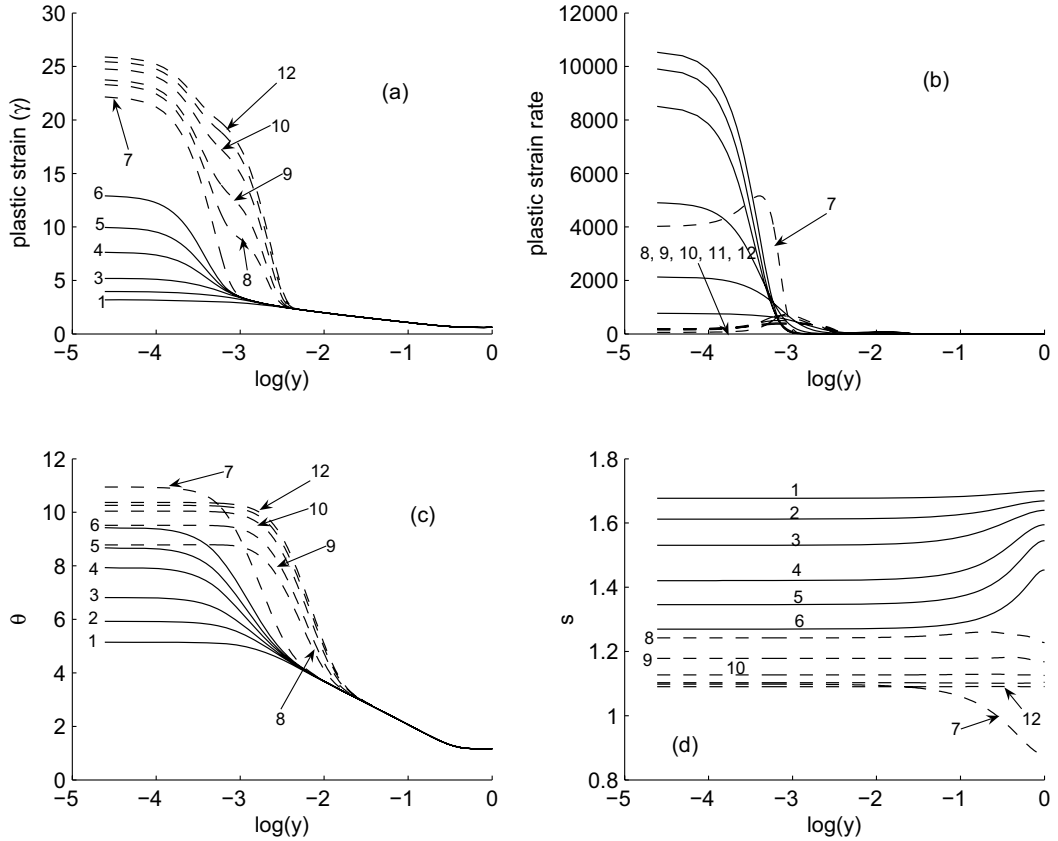

Figure 11: The spatial structure of field variables at selected points of time (a) plastic strain, (b) plastic strain rate, (c) temperature, (d) shear stress. The band narrowing stage (the solid curves) includes instants of t = 0.76963(1), 0.77020(2), 0.77056(3), 0.77091(4), 0.77116(5), 0.77145(6) and the band widening or post-localization stage (the dash curves) includes instants t = 0.77254(7), 0.78364(8), 0.78815(9), 0.79408(10), 0.79763(11), 0.80000(12).

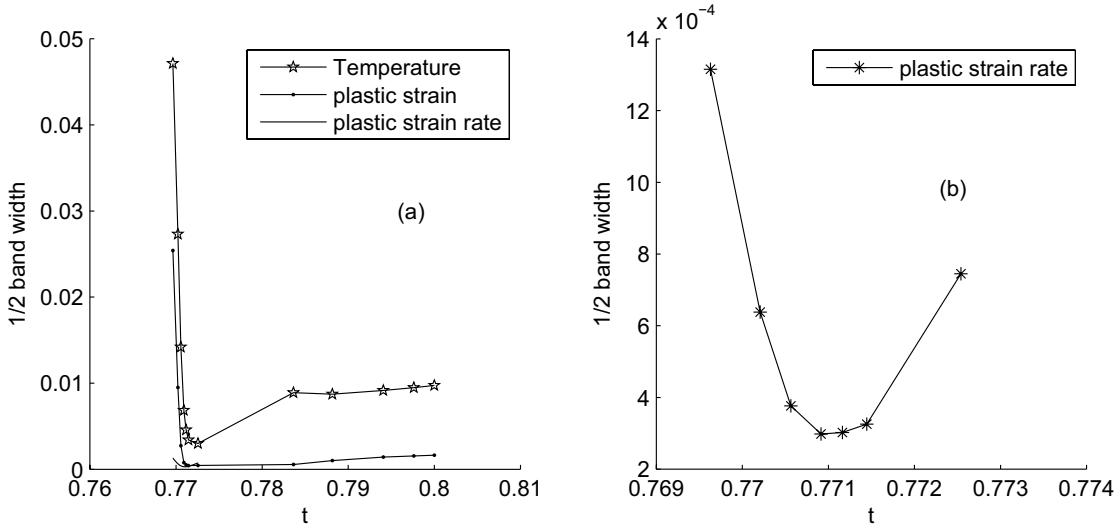

Figure 12: Evolution of bandwidths shows the band narrowing stage followed by the band widening stage, and the bandwidth based on the plastic strain rate is the narrowest while the one based on temperature is the widest.

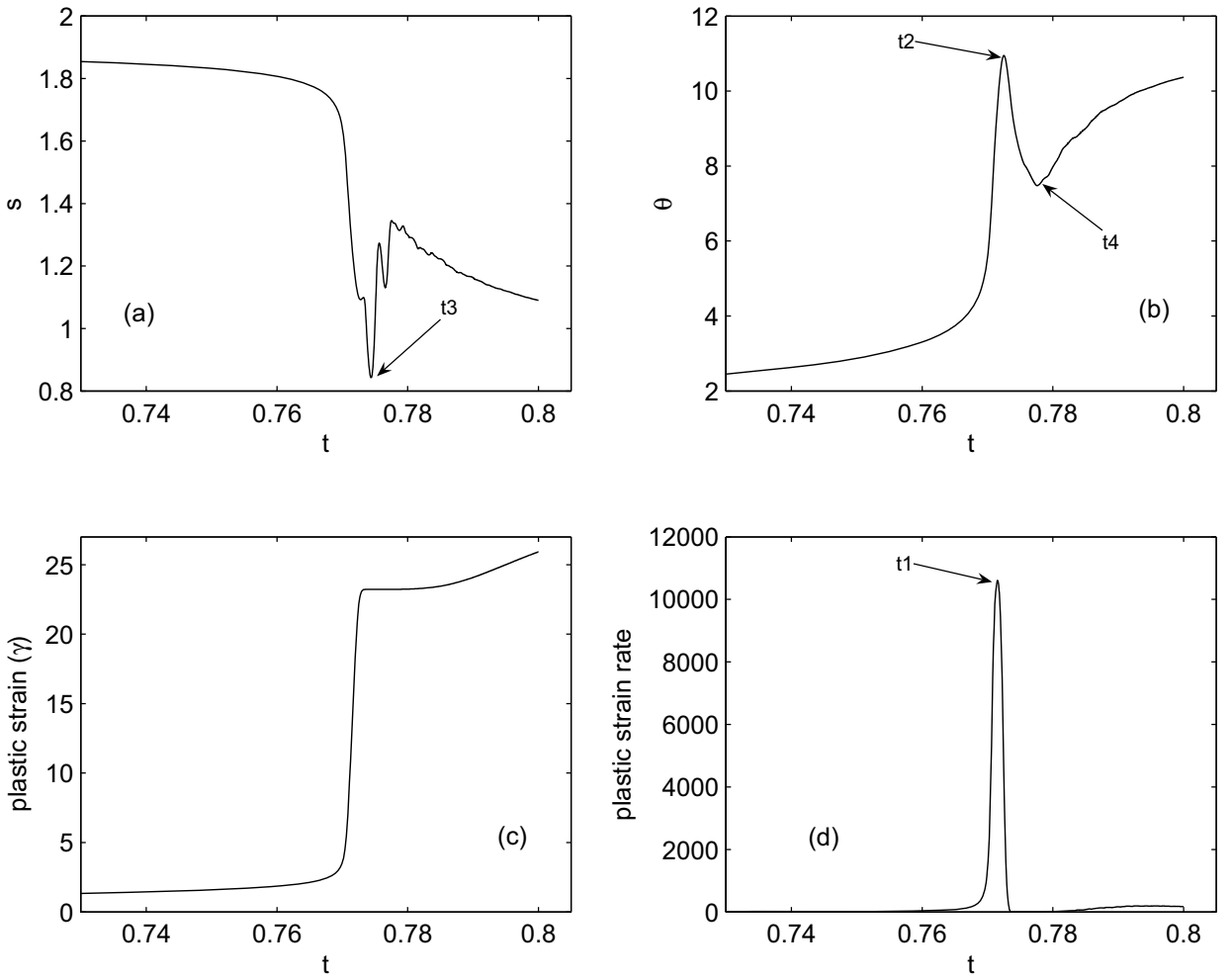

Figure 13: The evolution of (a) shear stress, (b) temperature, (c) plastic strain, (d) plastic strain rate at y = 0. A peak value of the plastic strain rate of 10606.778 occurs at $t_1 = 0.77154$, the temperature of 10.9490 at $t_2 = 0.77250$, the stress of 0.84238 at $t_3 = 0.77440$, and a second peak (local minimum of 7.4781) of temperature at $t_4 = 0.77759$. Thus $t_1 < t_2 < t_3 < t_4$.

the field variable profiles are self-similar. The band then widens in the second stage from around time instant $t = 0.77254$ (instant 7) onwards. The bandwidth evolution can be quantified by defining the extent of the bandwidth as the position where the value of a physical property (Θ, γ, or $\dot{\gamma}$) drops to 50% of its value at the band centre (here we use the 50% criterion in order to compare our results with those of Bayliss, Belytschko, Kulkarni, and Lott-Crumpler (1994)). The bandwidths are shown in Figure 12, confirming the band narrowing and widening stages as observed above, with the bandwidth for the plastic strain rate being the thinnest and for temperature the thickest. There is a smooth transitional region between the central shear band and the outer material where the plastic strain rate, plastic strain and temperature profiles remain virtually unchanged with time. However, the stress profile continues to evolve everywhere, with stress level generally dropping due to the softening effect, except some temporary hardening at the band centre (Figure 13).

Figure 13 shows the timing of key events during the process of strain localization. The plastic strain rate rises rapidly and attains its peak value at $t_1 = 0.77154$, followed by the temperature peaking at $t_2 = 0.77250$, and the stress at $t_3 = 0.77440$. By using the criterion Eq. 52 as

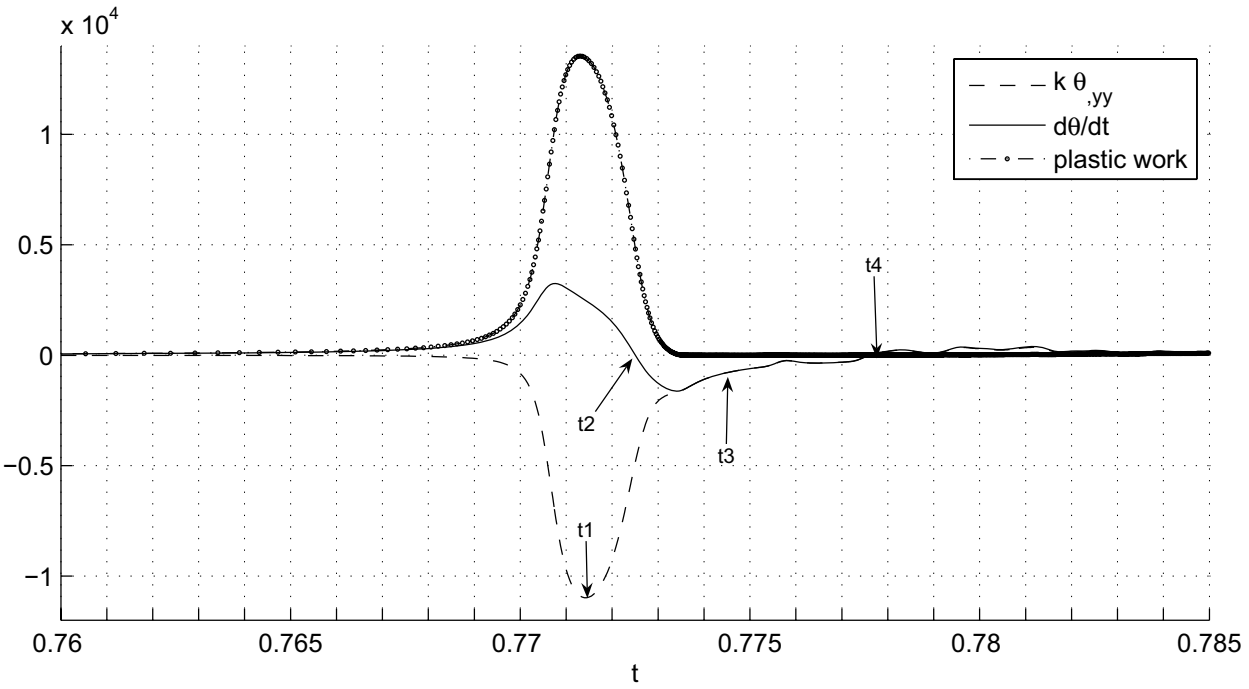

Figure 14: The interaction between thermal diffusion and plastic heating at $y = 0$: the dash curve depicts the evolution of the effect of thermal diffusion, $k\Theta_{,yy}$, dash-dot curve the effect of plastic heating $s\dot{\gamma}$, and the solid curve the combined effect $\frac{d\Theta}{dt} = k\Theta_{,yy} + s\dot{\gamma}$ of thermal diffusion and plastic heating. The onset of strain localisation occurs at $t = 0.76976$. Some key events occur at $t_1 = 0.77154 < t_2 = 0.77250 < t_3 = 0.77440 < t_4 = 0.77759$, as identified in the previous figure.

in example 1, the onset of localization is found to occur at $t = 0.76976$, which is when the rate of temperature increase starts to rise rapidly as shown in Figure 14. This figure also shows that the strength imperfection is such that the thermal diffusion process is much slower than the rate of heat generated by plastic work which causes rapid localised increase of Θ. The high temperature triggers a dramatic thermal softening process with a very brief period of elastic unloading. Although strain hardening becomes stronger briefly, thermal softening dominates and the band widens. Soon after the onset of localisation, $\dot{\gamma}$ at $y = 0$ reaches a peak value $\dot{\gamma}_{peak} = 10606.778$ at time $t = t_1 = 0.77154$ while the strain hardening parameter Ψ is still growing. At this time, Θ is still increasing and shear stress decreasing. After attaining the maximum value, $\dot{\gamma}$ drops rapidly to near zero then rises slowly. There are small oscillations in the behaviour of $\dot{\gamma}$ in this regime, which was also found in Bayliss, Belytschko, Kulkarni, and Lott-Crumpler (1994). As the plastic strain rate drops, the rate of plastic heating becomes slower and thermal diffusion becomes briefly dominant between $t_2 = 0.77250$ and $t_4 = 0.77759$ when the rate of plastic heating is again faster, causing further temperature rise. At $t = t_1 = 0.77154$ the bandwidths are 6.43×10^{-3}, 8.40×10^{-4}, 6.75×10^{-4} based on Θ, γ, $\dot{\gamma}$ respectively, which are compared with the corresponding values of 6.08×10^{-3}, 7.61×10^{-4}, 3.92×10^{-4} obtained by Bayliss, Belytschko, Kulkarni, and Lott-Crumpler (1994).

The evolution of plastic strain rate $\dot{\gamma}$, and temperature Θ in the localized region during the severe localization are visualised in Figure 15 and Figure 16 respectively. In Figure 17, the evolution of shear stress s over the whole domain is depicted. The spatial profile of the shear stress s is very uniform before the shear stress reaches its minimum at t_3, followed by mildly oscillatory behaviour, a behaviour not observed in the ther-

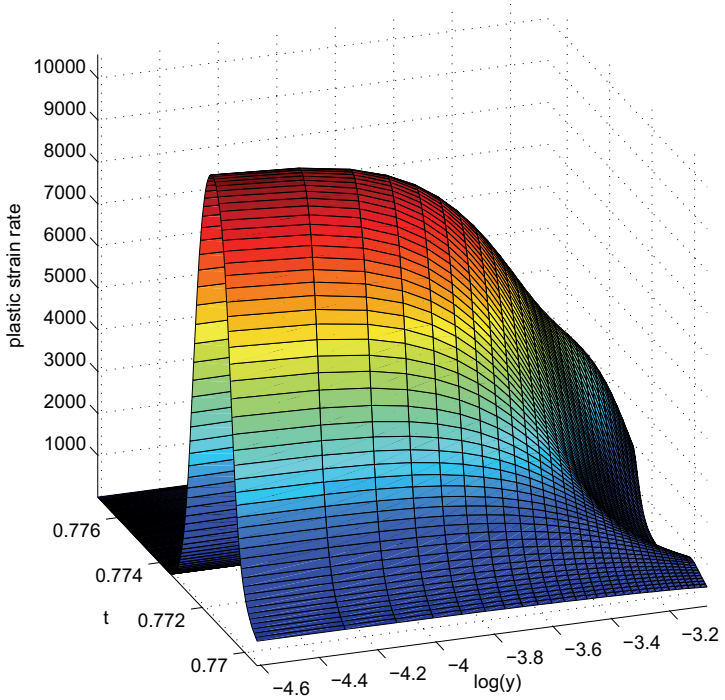

Figure 15: The evolution of plastic strain rate $\dot{\gamma}$.

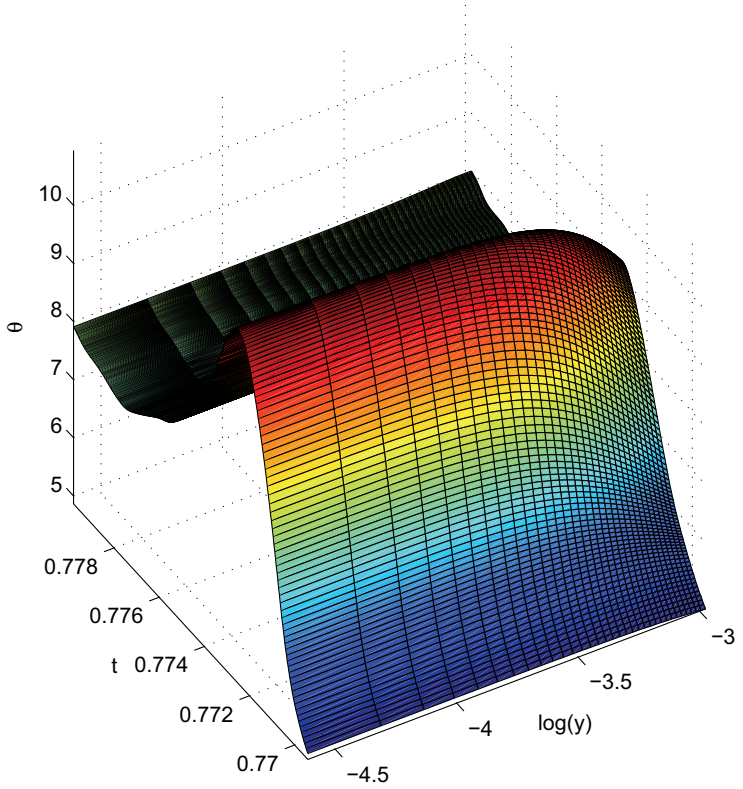

Figure 16: The evolution of temperature.

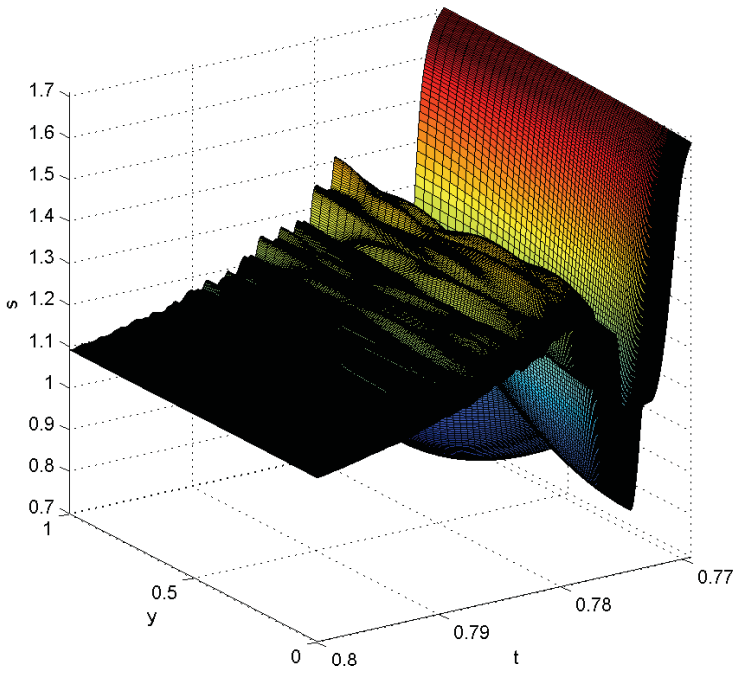

Figure 17: The evolution of shear stress.

mal imperfection model considered in example 1 above. The present results are compared with those obtained by the Modified Smooth Particle Hyrodynamics method (MSPH) [Batra and Zhang (2004)] and Chebyshev Pseudo Spectral method (CPS) [Bayliss, Belytschko, Kulkarni, and Lott-Crumpler (1994)] in Tables 1-2. Despite general qualitative agreement between the methods and some excellent quantitative agreements, there are some large differences between the numerical results. For the timing of key events, t_1, t_2, t_3, t_4, the present results fall between the MSPH and the CPS results and are much closer to the latter (within 7%), although the time lags $t_2 - t_1$, $t_3 - t_1$, $t_4 - t_1$ are virtually identical between the present IRBFN and the MSPH methods. In contrast, the results for $\dot{\gamma}_{peak}$, Θ_{peak}, s_{min}, Θ_{min}, γ_{t_1} and γ_{t_2} are much closer to those obtained by the MSPH method.

4.3 Convergence characteristics

For example 1, we use six discretisations ($\{N_i\}_{i=1}^{p=6} = \{61, 101, 141, 181, 221, 261\}$ uniformly spaced collocation points, i.e. spacing $h_i = 1/N_i$) to study the convergence of our method. Due to a lack of exact solution, an estimate of "error" is computed as follows. For each level of discretisation, the governing equations are integrated to a specified time instant just after the onset of localisation ($t = 60.507\mu$s and $t = 0.77115$ for example 1 and 2, respectively) to obtain the spatial profile of the temperature at this time instant. Then the temperatures at $Q = 300$ points are computed by interpolation (i.e. by the close form RBFN just found) and the discrete relative L_2 error is computed as

$$N_e = \sqrt{\frac{\sum_{j=1}^{Q}(\Theta_j^i - \Theta_j^p)^2}{\sum_{j=1}^{Q}(\Theta_j^p)^2}}, \quad i = 1, 2, \ldots, p-1,$$

where $p = 6$ for example 1 and 5 for example 2. Similarly, for example 2, we use five discretisations ($\{N_i\}_{i=1}^{p=5} = \{61, 101, 141, 181, 221\}$ uniformly spaced collocation points). Figure 18 shows that the "error" is proportional to $O(h^{2.48})$ and $O(h^{4.12})$ for example 1 and 2, respectively. If we set the error at 10^{-2}, we would need 143 collocation points for example 1, and 98 for example 2. In the case of example 1, Batra and Zhang (2004) used 442 nodes in their investigation by the FE and MSPH methods, while in the

Table 1: Comparison of the results between methods: The results obtained by the present IRBFN method are generally between those by the MSPH and the CPS methods, except for the case of Θ_{min} and γ_{t_1}.

	t_1	t_2	t_3	t_4	$\dot{\gamma}_{peak}$	Θ_{peak}	s_{min}	Θ_{min}	γ_{t_1}	γ_{t_2}
MSPH	0.9445	0.9455	0.9474	0.9505	11500	11	0.78	7.4	11	24
IRBFN	0.7715	0.7725	0.7744	0.7776	10606	10.95	0.84	7.48	14.0	22.1
CPS	0.7239	0.7252	0.7268	0.7284	5300	8.61	1.22	6.95	6.8	11.7

Table 2: Comparison of the time lags between methods: agreement is generally excellent, except that the CPS results show an ealier occurrence of the local temperature minimum.

	$t_2 - t_1$	$t_3 - t_1$	$t_4 - t_1$
MSPH	0.001	0.0029	0.0060
IRBFN	0.001	0.0029	0.0061
CPS	0.0013	0.0029	0.0045

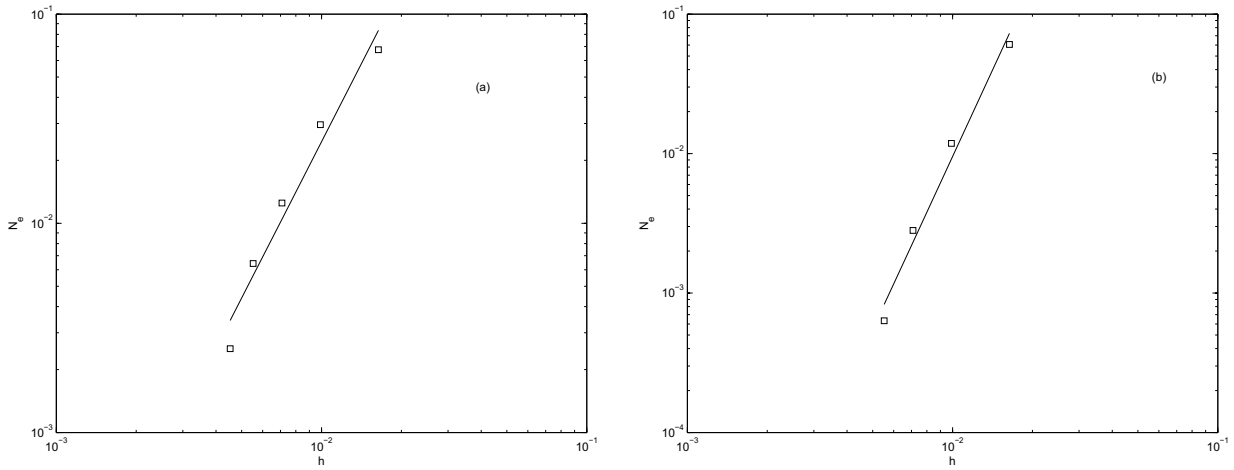

Figure 18: Convergence characteristics: (a) thermal imperfection model, (b) strength imperfection model.

case of example 2, Bayliss, Belytschko, Kulkarni, and Lott-Crumpler (1994) used 61 points in their CPS method.

5 Conclusion

We use the meshless IRBFN method to analyze the strain localization of an elasto-thermo-visco-plastic slab under simple shearing. We introduce a new coordinate mapping that allows very high resolution of the spatial structure of the resultant localised shear band with a relatively small number of computational degrees of freedom, distributed uniformly in the computational domain. The effects of elastic unloading, strain and strain rate hardening, thermal softening, heat conduction are considered. Either the thermal imperfection in the initial conditions or the strength imperfection in the constitutive relation can lead to severe strain localization, i.e. in a very narrow adiabatic shear band characterised by very high plastic strain rate, rapid increase of temperature and sudden drop of shear stress. The dynamics of formation and evolution as well as the spatial structures of the resultant adiabatic shear band are investigated. We define a criterion that allows a consistent determination of the onset of localization. The present results are compared favourably with those of the Modified Smooth Particle Hyrodynamics method [Batra and Zhang (2004)], and somewhat less efficient than the Chebyshev Pseudo Spectral method [Bayliss, Belytschko, Kulkarni, and Lott-Crumpler (1994)]. The governing equations are not integrated fur-

ther since we are not considering any fracture criterion. The application of the present method to two- and three-dimensional strain localisation problems will be carried out in our future work.

Acknowledgement: This work is supported by the Australian Research Council. This support is gratefully acknowledged.

References

Atluri, S.; Shen, S. (2002): The meshless local Petrov-Galerkin (MLPG) method:A simple & less-costly alternative to the finite element and the boundary element methods. *CMES: Computer Modeling in Engineering & Sciences*, vol. 3, pp. 11–51.

Atluri, S. N.; Zhu, T. (1998): A new meshless local Petrov-Galerkin (MLPG) approach in computational mechanics. *Comput. Mech.*, vol. 22, pp. 117–127.

Batra, R. C.; Kim, C. H. (1991): Effect of thermal conductivity on the initiation, growth and bandwidth of adiabatic shear bands. *International Journal of Engineering Science*, vol. 29, pp. 949–960.

Batra, R. C.; Zhang, G. M. (2004): Analysis of adiabatic shear bands in elasto-thermo-viscoplastic materials by Modified Smooth-Particle Hydrodynamics (SPH) method. *Journal of Computational Physics*, vol. 201, pp. 172–190.

Bayliss, A.; Belytschko, T.; Kulkarni, M.; Lott-Crumpler, D. A. (1994): On the dynamics and the role of imperfections for localization in thermo-viscoplastic materials. *Modelling and Simulation in Materials Science and Engineering*, vol. 2, pp. 941–964.

Hairer, E.; Norsett, S.; Wanner, G. (1987): *Solving Ordinary Differential Equations I. Non-stiff Problems*. Springer-Verlag.

Hairer, E.; Wanner, G. (1996): *Solving Ordinary Differential Equations II. Stiff and Differential-Algebraic Problems*. Springer-Verlag.

Han, Z.; Atluri, S. (2004): A meshless local Petrov-Galerkin (MLPG) approach for 3-diemensional elasto-dynamics. *CMC: Computers, Materials and Continua*, vol. 1, pp. 129–140.

Han, Z. D.; Atluri, S. N. (2003): Trully Meshless Local Petrov-Galerkin (MLPG) Solutions of Traction & Displacement BIEs. *CMES: Computer Modeling in Engineering & Sciences*, vol. 4, no. 6, pp. 665–678.

Han, Z. D.; Liu, H. T.; Rajendran, A. M.; Atluri, S. N. (2006): The Applications of Meshless Local Petrov-Galerkin (MLPG) Approaches in High-Speed Impact, Penetration and Perforation Problems. *CMES: Computer Modeling in Engineering & Sciences*, vol. 14, no. 2, pp. 119–128.

Han, Z. D.; Rajendran, A. M.; Atluri, S. N. (2005): Meshless Local Petrov-Galerkin (MLPG) Approaches for Solving Nonlinear Problems with Large Deformations and Rotations. *CMES: Computer Modeling in Engineering & Sciences*, vol. 10, no. 1, pp. 1–12.

Kansa, E. J. (1990): Multiquadrics – a scattered data approximation scheme with applications to computational fluid dynamics – II. Solutions to parabolic, hyperbolic and elliptic partial differential equations. *Computers & Mathematics with Applications*, vol. 19, pp. 147–161.

Kansa, E. J.; Power, H.; Fasshauer, G. E.; Ling, L. (2004): A volumetric integral radial basis function method for time-dependent partial differential equations: I formulation. *Engineering Analysis with Boundary Elements*, vol. 28, pp. 1191–1206.

Li, S.; Liu, W. C. (2000): Numerical simulation of Strain localization in inelastic solids using mesh-free method. *International Journal for Numerical Methods in Engineering*, vol. 48, pp. 1285–1309.

Ling, L.; Trummer, M. R. (2004): Multiquadratic collocation method with integral formulation for boundary layer problems. *Computers & Mathematics with Applications*, vol. 48, pp. 927–941.

Ling, L.; Trummer, M. R. (2006): Adaptive multiquadratic collocation for boundary layer problems. *Journal of Computational and Applied Mathematics*, vol. 188, pp. 265–282.

Madych, W. R.; Nelson, S. A. (1990): Multivariate interpolation and conditionally positive definite functions, II. *Mathematics of Computation*, vol. 54, pp. 211–230.

Mai-Cao, L.; Tran-Cong, T. (2005): A meshless IRBFN-based method for transient problems. *CMES: Computer Modeling in Engineering & Sciences*, vol. 7, pp. 149–171.

Mai-Duy, N. (2005): Solving high order ordinary differential equations with radial basis function networks. *International Journal for Numerical Methods in Engineering*, vol. 62, pp. 824–852.

Mai-Duy, N.; Tanner, R. I. (2005): Solving high order partial differential equations with indirect radial basis function networks. *International Journal for Numerical Methods in Engineering*, vol. 63, pp. 1636–1654.

Mai-Duy, N.; Tran-Cong, T. (2001): Numerical solution of differential equations using multiquadric radial basic function networks. *Neural Networks*, vol. 14, pp. 185–199.

Mai-Duy, N.; Tran-Cong, T. (2003): Approximation of function and its derivatives using radial basis function networks. *Applied Mathematical Modeling*, vol. 27, pp. 197–220.

Mai-Duy, N.; Tran-Cong, T. (2005): An efficient indirect RBFN-based method for numerical solution of PDEs. *Numerical Methods for Partial Differetial Equations*, vol. 21, pp. 770–790.

Mai-Duy, N.; Tran-Cong, T. (2006): Solving biharmonic problems with scattered-point discretization using indirect radial-basis-function networks. *Engineering Analysis with Boundary Elements*, vol. 30, pp. 77–87.

Molinari, A.; Clifton, R. J. (1987): Analytical characterization of shear localization in thermoviscoplastic materials. *Journal of Applied Mechanics*, vol. 54, pp. 806–812.

Rice, J. R.; Rudnicki, J. W. (1980): A note on some features of the theory of localization of deformation. *International Journal for Solids Strucrures*, vol. 16, pp. 597–605.

Sherif, R. A.; Shawki, T. G. (1992): The role of heat conduction during the post-localization regime in dynamic viscoplasticity. *Plastic flow and Creep, ASME*, vol. AMD-Vol. 135/MD-Vol. 31, pp. 159–173.

Tang, T.; Trummer, M. R. (1996): Boundary layer resolving pseudospectral methods for singular pertubation problems. *SIAM Journal of Scientific Computing*, vol. 17, pp. 430–438.

Walter, J. W. (1992): Numerical experiments on adiabatic shear band formation in one dimension. *International Journal of Plasticity*, vol. 8, pp. 657–693.

Wright, T. W. (1990): Adiabatic shear bands. *Journal of Applied Mechanics*, vol. 43, pp. S196–S200.

Wright, T. W. (2002): *The physics and mathematics of adiabatic shear bands*. Cambridge University Press.

Wright, T. W.; Walter, J. W. (1987): On stress collapse in adiabatic shear bands. *Journal of Mechanics and Physics of Solids*, vol. 35, pp. 701–720.